Research Square

Preprints are preliminary reports that have not undergone peer review.
They should not be considered conclusive, used to inform clinical practice,
or referenced by the media as validated information.

Rapid Antibiotic Susceptibility Testing by Reflectometric Interference Fourier Transform Spectroscopy on pH-responsive Hydrogel Infiltrated Porous Silicon Integrated into Microchips

Fereshteh Rahimi

rahimi.f@ut.ac.ir

School of Life Science Engineering, College of Interdisciplinary Science and Technology, University of Tehran

Shima Abarghoe

University of Tehran

Nizami Duran

Tayfur Ata Sökmen Faculty of Medicine, Hatay Mustafa Kemal University

Ali Abouei Mehrizi

Department of medical technology and tissue engineering

Mahsa Sedighi

Shahid Beheshti University

Mahya Mosayebzadeh

School of Life Science Engineering, College of Interdisciplinary Science and Technology, University of Tehran

Elif Yaprak Çolak

Tayfur Ata Sökmen Faculty of Medicine, Hatay Mustafa Kemal University

Selin Sabancı

Tayfur Ata Sökmen Faculty of Medicine, Hatay Mustafa Kemal University

---

Article

Keywords: Antimicrobial susceptibility testing, Reflectometric Interference Fourier Transform Spectroscopy, Gelatin, Porous Silicon, Concentration Gradient Generator, Microchip, Design, Simulation, 3D printing

Posted Date: September 23rd, 2026

DOI: https://doi.org/10.21203/rs.3.rs-10618547/v1

License: This work is licensed under a Creative Commons Attribution 4.0 International License.
Read Full License

Additional Declarations: There is no conflict of interest

Rapid Antibiotic Susceptibility Testing by Reflectometric Interference Fourier Transform Spectroscopy on pH-responsive Hydrogel Infiltrated Porous Silicon Integrated into Microchips

Shima Abarghoe[1], Fereshteh Rahimi[1*], Nizami Duran[2*], Ali Abouei Mehrizi[3], Mahsa Sedighi[4], Mahya Mosayebzadeh[3], Elif Yaprak Colak[2], Selin Sabanci[5]

[1] Department of Nanobiotechnology and Biomimetics, School of Life Science Engineering, College of Interdisciplinary Science and Technology, University of Tehran, Tehran, Iran, 1439957131.

[2] Department of Microbiology, Faculty of Medicine, Mustafa Kemal Hatay University, Antakya-Hatay, Turkey, 31060.

[3] Department of Medical Technology and Tissue Engineering, School of Life Science Engineering, College of Interdisciplinary Science and Technology, University of Tehran, Tehran, Iran, 1439957131.

[4] Converging Technologies Research Center, Shahid Beheshti University, Tehran, Iran, 19839-69411.

[5]Department of Histology and Embryology, Faculty of Medicine, Mustafa Kemal Hatay University, Antakya-Hatay, Turkey, 31060.

*Corresponding Authors:

Fereshteh Rahimi: orcid.org/0000-0003-0020-644X; Email: rahimi.f@ut.ac.ir, Phone: +982186093154

Nizami Duran: orcid.org/0000-0002-2766-3491; E-mail: nduran@mku.edu.tr; Phone: +905334675534

Abstract:

Rapid antimicrobial susceptibility testing is essential for timely therapeutic decision-making and limiting the global spread of antimicrobial resistance. However, conventional methods are labor-intensive and require prolonged incubation, delaying antibiotic selection. Here, we present a microfluidic–interferometric platform for rapid label-free antimicrobial susceptibility testing based on antibiotic-dependent bacterial metabolic acidification. A 3D-printed concentration gradient generator microchip was interconnected with a five-channel

microfluidic chip containing gelatin-infiltrated porous silicon Fabry–Pérot nanosensors. Scanning electron microscopy, energy-dispersive X-ray spectroscopy, and transfer matrix method simulations confirmed partial gelatin infiltration into the porous silicon layer. The simulations further revealed pH-dependent swelling of the infiltrated hydrogel within the pores, providing the basis for optical pH sensing. Acidification of the culture medium during *Escherichia coli* metabolism increased the effective optical thickness, which was continuously monitored by reflectometric interference Fourier transform spectroscopy. A pH calibration established using buffer solutions agreed well with bacteria-induced optical responses, confirming that the measured optical changes originated from metabolic acidification. The platform was then used to evaluate the susceptibility of *Escherichia coli* to ciprofloxacin, gentamicin, and ceftazidime. Results obtained after only 1.5 h showed strong agreement with those from 8 h of conventional incubation, yielding Pearson correlation coefficients of 0.92 for ciprofloxacin and gentamicin and 0.96 for ceftazidime. This platform accelerates antimicrobial susceptibility testing by combining rapid microfluidic analysis with on-chip generation and simultaneous incubation of multiple antibiotic concentrations. Together with label-free optical sensing and low sample consumption, these features make the proposed platform a promising approach for rapid antimicrobial susceptibility testing.

Keywords: Antimicrobial susceptibility testing, Reflectometric Interference Fourier Transform Spectroscopy, Gelatin, Porous Silicon, Concentration Gradient Generator, Microchip, Design, Simulation, 3D printing.

1. Introduction.

Despite remarkable advances in antimicrobial therapy, bacterial infections remain a leading cause of global morbidity and mortality. The increasing prevalence of multidrug-resistant

pathogens, particularly extended-spectrum β-lactamase producing *Escherichia coli (E. coli)*, has compromised empirical antimicrobial therapy and become a major challenge in clinical microbiology. Regional surveillance studies have revealed considerable variability in antimicrobial susceptibility and resistance gene dissemination, underscoring the dynamic nature of antimicrobial resistance and the need for continuous surveillance supported by rapid antimicrobial susceptibility testing (AST). Furthermore, the co-occurrence of disinfectant and antibiotic resistance genes further complicates infection control and antimicrobial stewardship, emphasizing the demand for rapid and reliable AST strategies[1,2]. Accordingly, timely identification of effective antimicrobial therapy is essential for improving patient outcomes and reducing infection-related mortality. In 2021, bacterial antimicrobial resistance was associated with 4.71 million deaths worldwide, with 1.14 million deaths directly attributable to bacterial resistance. This number is projected to rise to 1.91 million annually by 2050 [3,4]. These findings underscore the need for rapid AST to guide timely therapy and curb antimicrobial resistance.

AST is essential for optimizing therapy, minimizing broad-spectrum antibiotic use, and limiting antimicrobial resistance. Although conventional phenotypic methods, including disk diffusion, broth dilution, and E-tests, remain the clinical gold standard because they directly evaluate bacterial growth inhibition, they have inherent limitations [1,5]. These labor-intensive methods require large bacterial inocula and more than 24 h to yield reliable results [6,7] . The long turnaround time necessitates empirical therapy, highlighting the need for rapid AST platforms to monitor bacterial metabolism and guide targeted antimicrobial therapy [8].

Various rapid AST platforms have been developed, including SERS [9], nanomotion detection [10], single-cell spectroscopy [11,12], nanowire sensors [13], and electrochemical sensing [14]. However, their clinical translation remains limited by complex instrumentation, extensive assay

77 optimization, and insufficient robustness, highlighting the need for practical rapid AST
78 platforms.

79 Microfluidic systems enable precise fluid control, low reagent consumption, rapid mass
80 transfer, and integration of multiple analytical steps within compact devices [15-17].
81 Concentration gradient generator microchips (CGG μchips) further allow automated
82 generation of antibiotic dilution series for parallel testing of multiple concentrations. However,
83 many microfluidic AST platforms still depend on fluorescent labels, complex imaging, or
84 bulky instrumentation, highlighting the need for label-free strategies that directly monitor
85 bacterial metabolic activity [18,19].

86 Stimuli-responsive hydrogels have emerged as promising biosensing materials because of their
87 porous structure and responsiveness to environmental stimuli [20,21]. Among these, pH-
88 responsive hydrogels are particularly attractive because they undergo swelling and shrinkage
89 through the protonation and deprotonation of their ionizable groups [22-26]. Since bacterial
90 metabolism acidifies the surrounding medium, the swelling behavior of these hydrogels can
91 serve as an indirect optical indicator of bacterial growth and metabolic activity [22,27].

92 Optically active nanostructures provide an effective strategy for converting biochemical
93 changes into measurable optical signals. Among these materials, porous silicon (PSi) is a
94 versatile label-free sensing platform owing to its large surface area, tunable pore structure, and
95 straightforward surface functionalization. As Fabry–Pérot thin films, PSi structures detect
96 refractive index changes within the porous matrix through variations in effective optical
97 thickness (EOT), which can be monitored by reflectometric interference Fourier transform
98 spectroscopy (RIFTS) [28-31]. The integration of a pH-responsive hydrogel layer with porous
99 silicon enables the conversion of bacterial metabolism-induced pH changes into measurable

optical signals. Recent studies have demonstrated the potential of porous silicon–hydrogel biosensors for monitoring bacterial growth [32] and AST [27].

Here, we present an integrated microfluidic–interferometric platform for AST. A 3D-printed CGG μchip was integrated with a microfluidic chip containing gelatin-infiltrated PSi (GIPSi) Fabry–Pérot nanosensors, enabling automated generation of antibiotic concentration gradients and label-free optical monitoring of bacterial growth. In this platform, bacterial metabolism acidifies the surrounding medium, inducing pH-dependent swelling of gelatin within the PSi matrix and corresponding changes in EOT, which are monitored by RIFTS. Transfer matrix method (TMM) simulations further supported the proposed sensing mechanism. Unlike the previously reported bilayer configuration, in which a pH-responsive chitosan hydrogel was coated on top of PSi for AST [27], the present sensing mechanism is based on a different structural configuration and optical response. The platform was validated using *E. coli* to determine the minimum inhibitory concentrations (MICs) of ciprofloxacin (CIP), gentamicin (GEN), and ceftazidime (CEF), demonstrating a compact, low-volume, and rapid strategy for parallel AST with potential clinical applicability[33].

2. Materials and methods.

All materials used are detailed in the Supporting Information file.

2.1. Fabrication of GIPSi

For preparation of GIPSi as a sensing element, the PSi layer was fabricated, oxidized, laser-cut into segments of approximately 0.8 mm × 8 mm and functionalized by (3‑aminopropyl) triethoxysilane according to a previously reported protocol [29] as shown in **Fig. 1a**. Then, a 4% (w/v) gelatin solution was prepared in deionized water and stirred at 40 °C for 1 h. Once the gelatin was fully dissolved, glutaraldehyde (2.5%, v/v) was added dropwise as a cross‑linker

(**Fig. 1b**). Before gelation was complete, 2 µL of the solution was deposited onto the modified PSi surface, where glutaraldehyde covalently reacted with surface amine groups [34]. The samples were dried at room temperature for 24 h (**Fig. 1c**).

2.2. Design, simulation and fabrication of CGG µchip

The CGG µchip was designed to generate precise concentration gradients of bacteria–antibiotic mixtures for downstream biosensing. The design concept is based on controlled splitting and recombination of two inlet streams to produce stable concentration gradients while maintaining compact device dimensions and low sample consumption. The µchip consists of two primary functional regions: a flow-divider region, responsible for distributing the inlet streams with predefined ratios, and a mixer region, which ensures efficient mixing and stable gradient formation. In the divider section, microchannels with different widths were used to regulate the flow distribution and produce specific concentration ratios, while the inlet positions were adjusted to compensate the hydraulic resistance differences and maintain balanced flow paths. To further enhance mixing performance within a compact footprint, a passive micromixer based on repeated contraction–expansion structures was incorporated to promote interfacial stretching and fluid layer folding.

The geometry of the microfluidic chip was designed using SolidWorks software, version SP5.0, 2022 (Dassault Systems, Paris, France). The flow behavior and concentration distribution inside the µchip were then evaluated through computational fluid dynamics simulations using COMSOL Multiphysics version 6.2. The simulations employed the laminar flow model coupled with the diluted species transport module to describe the hydrodynamics and mass transport within the microchannels. Fluid behavior within the microchannels is precisely modeled by employing the governing equations such as Navier-Stokes equations, as detailed in Eq. (1) and Eq. (2) and a mesh independence study was conducted to ensure

numerical accuracy. Following numerical validation of the design, the CGG μchip was fabricated using a resin-based stereolithography 3D printing technique. The printed μchips were subsequently cleaned with isopropyl alcohol to remove uncured resin, followed by ultrasonic cleaning and air flushing to clear the microchannels. Finally, surface polishing was performed to improve optical clarity and ensure proper functionality of the microfluidic chip.

$$\nabla . v = 0 \tag{1}$$

$$\frac{\partial v}{\partial t} + \rho(v.\nabla)v = -\nabla P + \mu\nabla^2 v \tag{2}$$

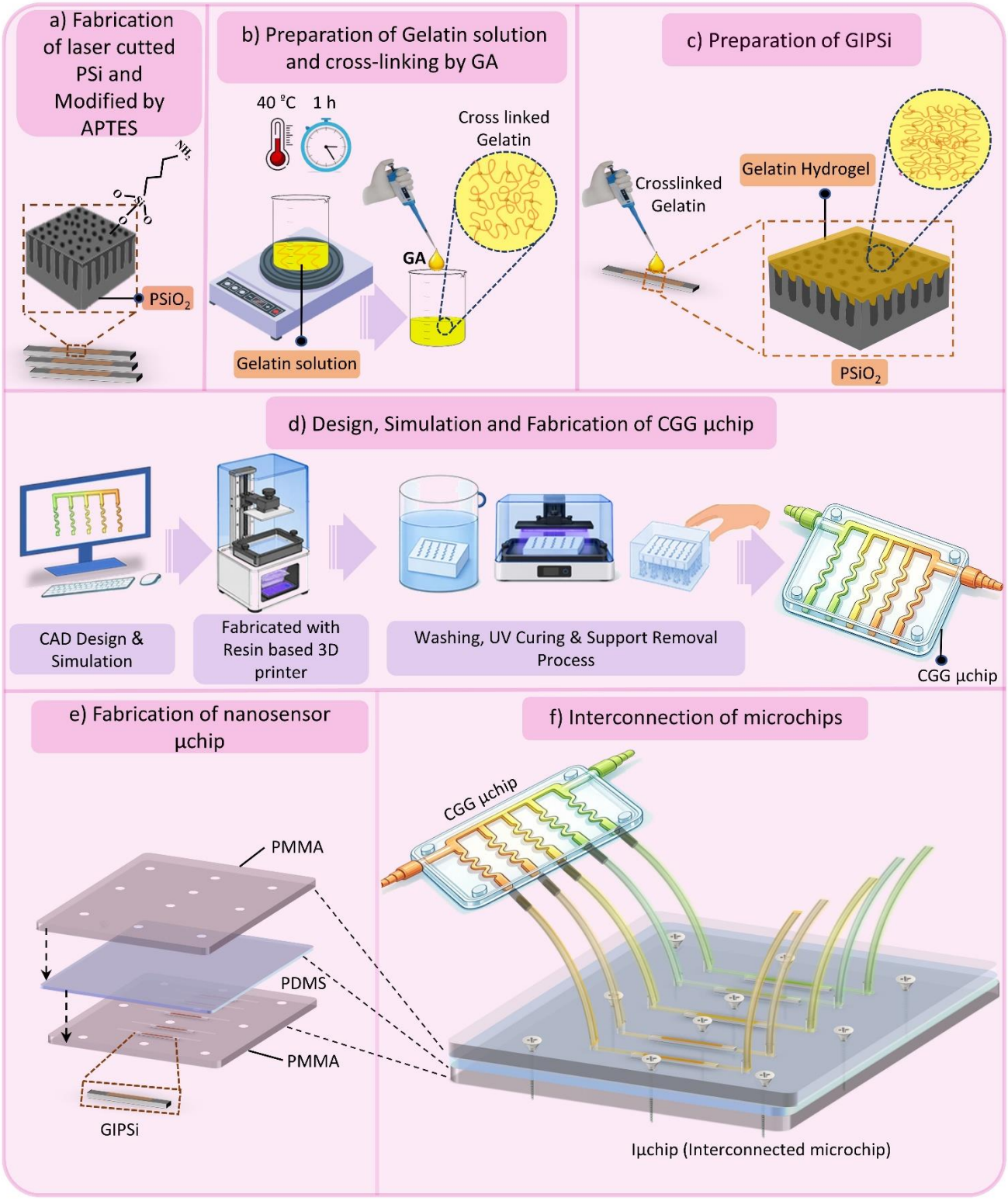
where p denotes the pressure, v represents the velocity vector, ρ is the density, ∇relates to the divergence, and (μ) refers to the dynamic viscosity (**Fig. 1d**). The design, simulation, and fabrication of the CGG μchip have been reported in detail elsewhere [35]. However, before conducting the experiments presented in this study, the functionality of the μchip was verified to ensure its proper operation (see **Fig. S1** in the Supplementary Information).

2.3. Fabrication of nanosensor μchip

The nanosensor μchip was designed and fabricated based on our previously reported three-layer, reversibly bonded architecture [29]. While the previous chip used a single inlet distributing flow into three parallel channels, the present chip incorporates five independent channels, each with its own inlet and outlet. This design allows separate introduction of different samples or reagents into each nanosensor zone. The fabrication process remained identical: micro-CNC machining of PMMA, application of a PDMS bonding layer (1 mm thickness), and mechanical clamping using M2 screws. As reported in our the previous work [29], each channel includes a precisely milled biosensing zone for the placement of PSi or GIPSi samples (**Fig. 1e**).

2.4. Interconnection of the nanosensor µChip with the CGG µChip

To establish fluidic coupling between the two µchips, the CGG one was fluidically interconnect in series with the five-channel nanosensor one. Each outlet of the CGG µchip was connected to the corresponding inlet of the nanosensor µchip using flexible microfluidic tubing, allowing independent delivery of the concentration-gradient mixtures generated from the two input samples to spatially separated biosensing regions. Prior to final assembly, the GIPSi sensing elements were positioned within the micromachined sensing chambers of the nanosensor µchip (see **video** in the Supplementary Information). The interconnected platform was mechanically clamped to maintain channel alignment and ensure leak-free operation. Before each experiment, the interconnected microchip (Iµchip) was flushed with buffer solution to eliminate trapped air bubbles and confirm stable flow through all channels. This Iµchip enabled simultaneous exposure of the GIPSi sensing elements to different concentrations of the target sample, allowing real-time optical monitoring (**Fig. 1f**).



180

181 **Figure 1. Illustration of the fabrication process leading from GIPSi to the Iµchip**

182

2.5. Characterization methods of GIPSi

The microstructural characterization of the samples was carried out using a field-emission scanning electron microscope (FE‑SEM, TESCAN MIRA3, Czech Republic) working at 15 kV acceleration voltage of the electron gun. To evaluate gelatin infiltration into the pores, energy‑dispersive X‑ray spectroscopy (EDX, SAMx, France) coupled with SEM was employed to determine the elemental composition. The surface chemical functionalization was confirmed by attenuated total reflectance‑Fourier transform infrared spectroscopy (ATR‑FTIR, UATR 2, PerkinElmer, USA) over the wavenumber range of 400–4000 cm^{-1}.

2.6. Optical setup and RIFTS measurement

RIFTS was used for optical transduction. The EOT, obtained from the Fourier transform of the reflectance spectrum, served as the sensing signal, and sensor responses were quantified as changes in EOT (ΔEOT, see Section 3.2, " Combined Experimental and Simulation Study of the pH-Sensing Mechanism "). The optical setup and data analysis protocol were identical to those described in our previous work. A motorized translation stage automatically positioned the five samples in the Iμchip beneath the optical probe, enabling sequential EOT measurements under identical optical conditions [29] (**Fig. 2**).

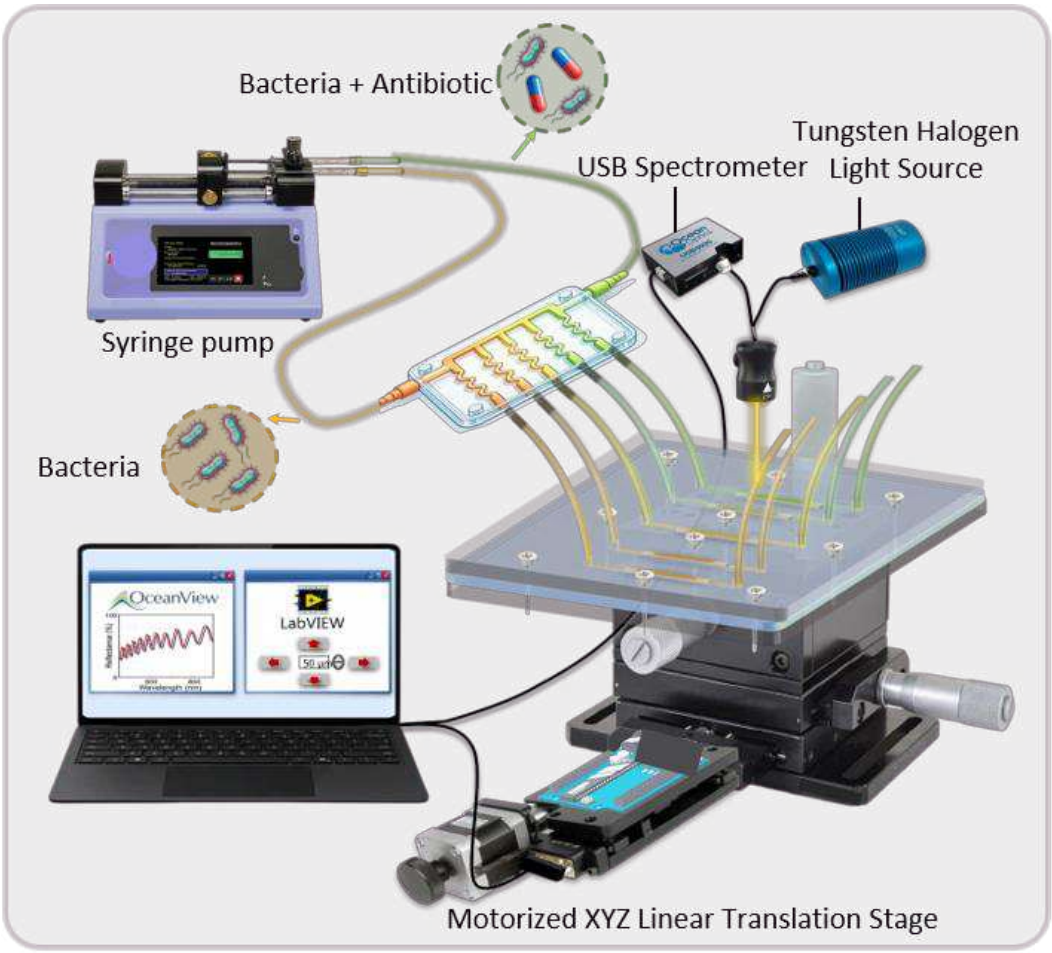


Figure 2. RIFTS system integrated with a motorized XYZ translation stage.

2.7. Simulation of reflectance spectra and their Fourier-transformed profiles

The reflectance spectra of single-layer and multilayer structures were simulated using the TMM. For each layer, the refractive index and thickness were used as input parameters, and the wavelength-dependent reflectance was calculated accordingly. The simulations were performed by MATLAB software (MathWorks Inc., Natick, MA, USA). To simplify the model, absorption was neglected, and a constant, real-valued refractive index was assumed over the entire wavelength range. In other words, dispersion was not taken into account, and no wavelength dependence of the refractive index was considered. The simulated reflectance spectra obtained from MATLAB were subsequently imported into IGOR Pro software, where

fast Fourier transform (FFT) analysis was performed to extract the corresponding Fourier-domain profiles.

2.8. Preparation of *E. coli* culture

E. coli was streaked onto nutrient agar using a four-quadrant streaking method and incubated aerobically at 37 °C for 18–24 h to obtain well-isolated colonies. Fresh overnight cultures were used throughout the study. Prior to each experiment, colony morphology was visually inspected to confirm culture purity, and well-isolated colonies were selected to minimize physiological variability and ensure experimental reproducibility. A single isolated colony was inoculated into Mueller-Hinton broth (MHB) supplemented with 2% (w/v) glucose and thoroughly homogenized. The bacterial suspension was standardized to a 0.5 McFarland turbidity standard by spectrophotometric measurement at 600 nm (OD600 = 0.08–0.10), corresponding to an inoculum of approximately 1.5×10^8 CFU/mL [36]. The standardized inoculum was prepared immediately before each experiment to minimize inoculum variability associated with bacterial growth phase.

2.9. MIC measurements

The MICs of CIP, GEN, and CEF were determined using the standard broth microdilution method following the CLSI M07 guidelines [36]. Fresh overnight bacterial cultures were resuspended in sterile physiological saline, and the turbidity was adjusted to the 0.5 McFarland standard. Serial two-fold dilutions of each antibiotic were prepared in cation-adjusted Mueller–Hinton broth (CAMHB) in 96-well plates. The antibiotic dilutions were inoculated with the standardized bacterial suspension to achieve a final bacterial density of approximately 5×10^5 CFU/mL in each well. Two control conditions were included in every assay: a positive growth control containing CAMHB and bacterial inoculum without antibiotic, and a negative sterility control containing CAMHB and antibiotic without bacterial inoculum. The plates were

incubated at 37 °C for 18–24 h. The MIC was defined as the lowest antibiotic concentration at which complete inhibition of visible bacterial growth was observed. MIC endpoints were independently evaluated by two investigators based on visual inspection after incubation, and all assays were performed in three independent biological experiments with technical replicates to confirm reproducibility.

2.10. RIFTS-based microfluidic experimental procedure

Before each experiment, the microfluidic chips, tubing, syringes, and connectors were disinfected with 70% ethanol, followed by 15 min of UV irradiation. All microbiological procedures were performed under aseptic conditions using sterile consumables. Syringes were mounted on programmable syringe pumps, and all solutions were delivered through the microfluidic chips at a constant flow rate of 500 μL min^{-1}.

For all RIFTS measurements, each GIPSi sensor was first equilibrated with an appropriate reference solution at pH 7.4 to establish a stable baseline EOT. Depending on the experiment, the reference solution consisted of PBS, culture medium, or a bacterial suspension adjusted to pH 7.4. The corresponding test solution was then introduced into the nanosensor μchip or Iμchip, and the resulting changes in effective optical thickness (ΔEOT) were calculated relative to the baseline EOT recorded under the corresponding reference condition.

Between successive measurements, the microfluidic channels were thoroughly rinsed with sterile deionized water, followed by the corresponding buffer or culture medium. Immediately before injection, bacterial suspensions were gently mixed to ensure homogeneous cell distribution and minimize sedimentation during flow through the microchannels.

For antimicrobial susceptibility testing, bacterial suspensions were adjusted to 1.5×10^8 CFU/mL, and antibiotic solutions were freshly prepared before each experiment. The device

was incubated at 37 °C for 1.5 h to evaluate concentration-dependent bacterial growth inhibition. Particular care was taken to avoid bubble formation and bacterial sedimentation, which could affect concentration gradients and the resulting optical responses. All experiments were conducted under controlled aseptic conditions optimized for rapid microfluidic AST measurements [37,38].

2.11. Statistical Analysis

All microbiological experiments were performed in at least three independent biological replicates, each including technical replicates where appropriate. Data are presented as mean ± standard deviation. Regression analyses were conducted using SigmaPlot software version 15 (Systat Software Inc.).

3. Results and discussion

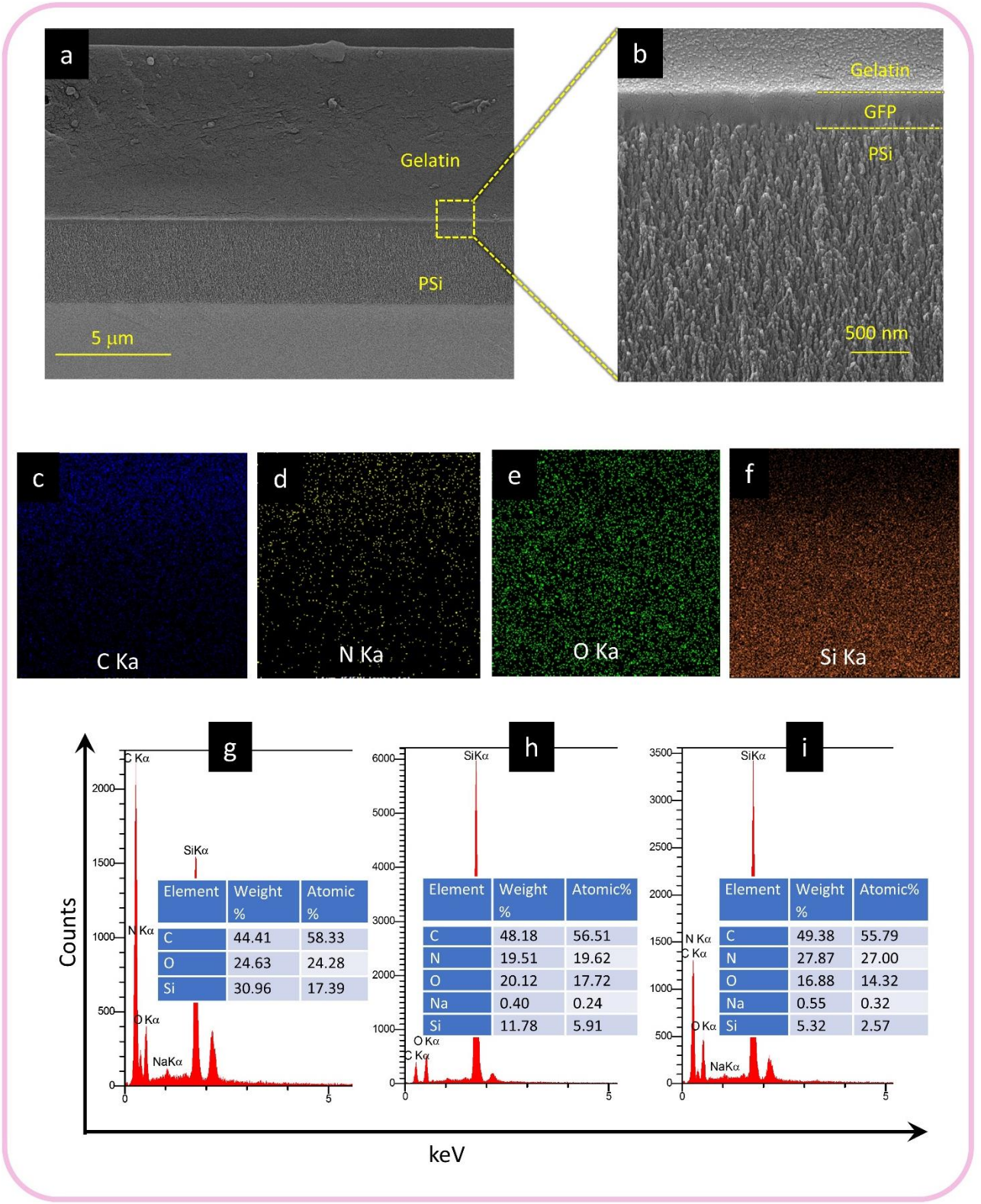
3.1 Characterization of GIPSi

A cross-sectional SEM image of a gelatin layer deposited on a PSi substrate is presented in **Fig. 3a**, while **Fig. 3b** shows a higher-magnification view of the region, revealing three distinct layers: a top gelatin layer, a bottom PSi layer, and an intermediate composite region designated as the Gelatin-filled Pores (GFP), formed by the penetration of gelatin into the PSi matrix. From the cross-sectional SEM image, the thicknesses of the PSi, GFP, and gelatin layers are in the ranges of 3.47–3.51 μm, 250-265 nm, and 7.76–7.79 μm, respectively.

To confirm the composite nature of this intermediate region and to distinguish it from the top gelatin layer, EDX elemental mapping was performed in the magnified region. The elemental distribution maps (**Fig. 3c–f**) correspond to carbon (C), nitrogen (N), oxygen (O), and silicon

(Si), respectively. The maps reveal a gradual decrease in C and N signals and a concomitant increase in the silicon signal from the top toward the bottom of the cross-section.

In addition, point EDX spectra were acquired from each of the three layers (**Fig. 3g–i**), along with their corresponding quantitative elemental compositions (shown as inset tables). The quantitative results further confirm the distinct chemical composition of the intermediate layer, which contains contributions from both gelatin-related elements (C and N) and the substrate-related element (Si). In contrast, the top layer is dominated by C and N, whereas the bottom layer consists predominantly of Si. These findings provide direct evidence for the formation of an interpenetration zone between the gelatin coating and the PSi matrix.



288

289 **Figure 3. Physicochemical characterization of GIPSi. a**) Cross-sectional SEM image of a gelatin-coated PSi

290 structure. **b**) The inset shows a magnified view of the selected region, revealing a top gelatin layer, a bottom PSi

layer, and an intermediate composite layer formed by gelatin infiltration into the Psi matrix. (**c–f**) EDX elemental maps of C, N, O, and Si, and (**g–i**) point EDX spectra from the gelatin layer, the composite layer and the PSi layer.

While SEM and EDX analyses provide structural and elemental evidence of GIPSi, ATR-FTIR spectroscopy was additionally employed to verify the chemical interaction between gelatin and the APTES-modified PSi surface and to examine the corresponding changes in surface functional groups (see **Fig. S2** in the Supplementary Information).

3.2 Combined Experimental and Simulation Study of the pH-Sensing Mechanism

To investigate the pH-responsive sensing mechanism, the reflectance spectra and corresponding Fourier-transform profiles of GIPSi were simulated using the TMM [39]. Simulations assumed normal incidence, a wavelength-independent refractive index, and zero optical absorption. Subsequently, the FFT of these simulated reflectance spectra was extracted using the IGOR software.

The simulation comprised four steps. Step a determined the porosity and thickness of oxidized PSi using TMM and SLIM, and step b modeled gelatin infiltration. Steps c and d simulated GIPSi at pH 6 and pH 8, respectively, as these conditions produced more pronounced spectral changes than pH 7.4.

Fig. 4a–d presents the corresponding simulation steps. In panel i of each subfigure, a schematic illustration of the sample structure is provided. Panel ii shows the layer thicknesses and refractive indices used in the simulations. Panel iii compares the experimentally measured reflectance spectrum with the simulated spectrum, whereas panel iv displays the Fourier-transformed experimental spectrum together with its simulated counterpart. A detailed description of each simulation step is provided below.

The optical properties of the oxidized PSi layer (**Fig. 4a-i**), including its thickness, porosity, and refractive index, were first determined. Reflectance spectra measured in air, methanol, and

ethanol were analyzed using the spectroscopic liquid infiltration method (SLIM) combined with the Bruggeman effective medium approximation [40,41], as described previously [29]. The extracted thickness agreed well with the SEM measurements and, together with the corresponding refractive indices (**Fig. 4a-ii**), was used to simulate the reflectance spectrum. As shown in **Fig. 4a-iii**, the simulated and experimental spectra exhibited good agreement, particularly in the 600–700 nm wavelength range. These discrepancies are mainly attributed to the assumption of wavelength-independent refractive indices, which were determined within this spectral range. Differences in peak amplitudes are further associated with the neglect of optical absorption in the model. The corresponding FFT spectra (**Fig. 4a-iv**) also showed excellent agreement, with nearly identical EOT peak positions.

In the second step, the reflectance spectrum and corresponding Fourier transform of the GIPSi structure (**Fig. 4b-i**) were simulated. The initial gelatin thickness was estimated from the SEM images (**Fig. 3**), while its refractive index was taken from the literature. The layer thicknesses and refractive indices were then iteratively optimized to obtain the best agreement between the simulated and experimental FFT spectra. The optimized structural parameters are shown in **Fig. 4b-ii**. The simulated reflectance spectrum agreed well with the experimental spectrum over the 500–1000 nm range (**Fig. 4b-iii**), confirming the validity of the optical model. The corresponding FFT spectra also showed excellent agreement (**Fig. 4b-iv**). The positions of the EOT peaks corresponding to the individual layers, as well as their combined optical contributions, are also indicated in the figure. Notably, the EOT peak at 33,892 nm was accurately reproduced only when the gelatin (GIPSi) layer was included in the model, confirming its essential role in the optical response. Excluding this layer resulted in a significant shift of the corresponding peak from its experimentally observed position.

Two points should be noted. First, the higher refractive index assigned to the PSi layer (1.491 vs. 1.441) reflects the APTES functionalization performed before gelatin deposition, which

increases the effective refractive index [29,30]. Second, the optimized refractive index of gelatin (1.459) is slightly lower than reported literature values (1.47–1.53) [42], possibly due to pore formation during drying. Another important observation concerns the refractive index of the gelatin-infiltrated porous layer. The Bruggeman effective medium approximation predicts an effective refractive index of 1.798, whereas the optimized simulation yielded 1.752. The lower value suggests incomplete gelatin infiltration, possibly resulting from shrinkage during drying.

Since the gelatin used in this study was Type A gelatin, whose isoelectric point lies in the range of 7-9 [43], a substantially higher degree of swelling is expected at pH 6 than at pH 8 [44]. Based on this behavior, schematic illustrations of the GIPSi structure under acidic (pH 6) and basic (pH 8) conditions are presented in **Figs. 4c-i** and **4d-i**, respectively.

As the gelatin layer absorbs the buffer solution and swells, the EOT peak associated with this layer is expected to shift toward higher optical thickness values in the FFT spectrum. However, no distinct peak attributable to the swollen gelatin layer could be identified above the background noise (**Figs. 4c-iv** and **4d-iv**). Simulation results indicate that, to reproduce this observation, the refractive index of the swollen gelatin layer must be lower than 1.339 under both acidic and basic conditions, thereby preventing the appearance of a well-defined FFT peak. Furthermore, simulations performed using refractive indices below 1.339 and layer thicknesses greater than 7760 nm produced no significant changes in the remaining spectral features. The remaining layer thicknesses and refractive indices (**Figs. 4c-ii** and **4d-ii**) were optimized to satisfy two fitting criteria simultaneously: (i) the simulated reflectance spectra should reproduce the peak and valley positions of the experimental spectra with the highest possible accuracy (**Figs. 4c-iii** and **4d-iii**), and (ii) the simulated FFT spectra should reproduce the position of the dominant EOT peak, while all other peaks remain below the experimental noise floor (**Figs. 4c-iv** and **4d-iv**).

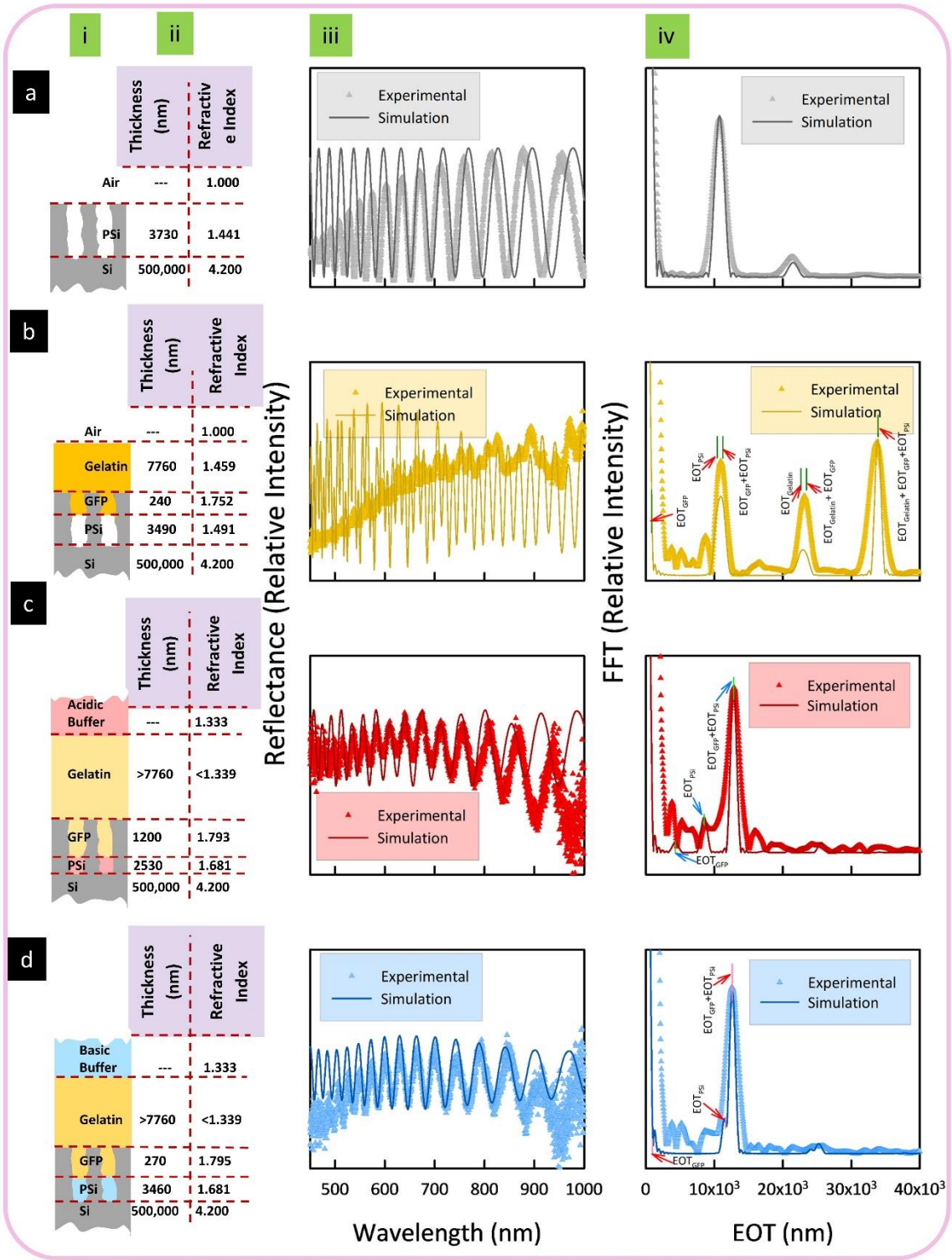


Figure 4. Experimental validation of the four-step optical simulation of the GIPSi pH sensor. (**a**) Oxidized PSi, (**b**) GIPSi, (**c**) GIPSi exposed to pH 6, and (**d**) GIPSi exposed to pH 8. For each simulation step, panel i shows

the schematic structure, panel ii the optimized optical parameters (layer thicknesses and refractive indices), panel iii the comparison between simulated and experimental reflectance spectra, and panel iv the comparison between the corresponding FFT spectra. The agreement between experiment and simulation validates the proposed optical model and the extracted structural parameters.

Based on the combined experimental observations and simulation results, the following mechanism is proposed for the pH-sensing response. As the pH of the surrounding buffer decreases, the thickness of the GFP increases due to swelling, while its effective refractive index decreases. Nevertheless, the increase in layer thickness outweighs the reduction in refractive index, resulting in an overall increase in the EOT of the GFP layer. Conversely, under basic conditions, the gelatin undergoes less swelling, leading to a reduction in its thickness and an increase in its effective refractive index. The net effect is a decrease in the EOT of the GFP layer.

As will be demonstrated in the following sections, bacterial growth also increases the EOT of the GFP layer through the pH changes induced by bacterial metabolism. In contrast, when an effective antibiotic inhibits bacterial growth, the associated pH change is suppressed, resulting in a decrease in the measured EOT compared with untreated bacterial cultures (**Fig. 5**).

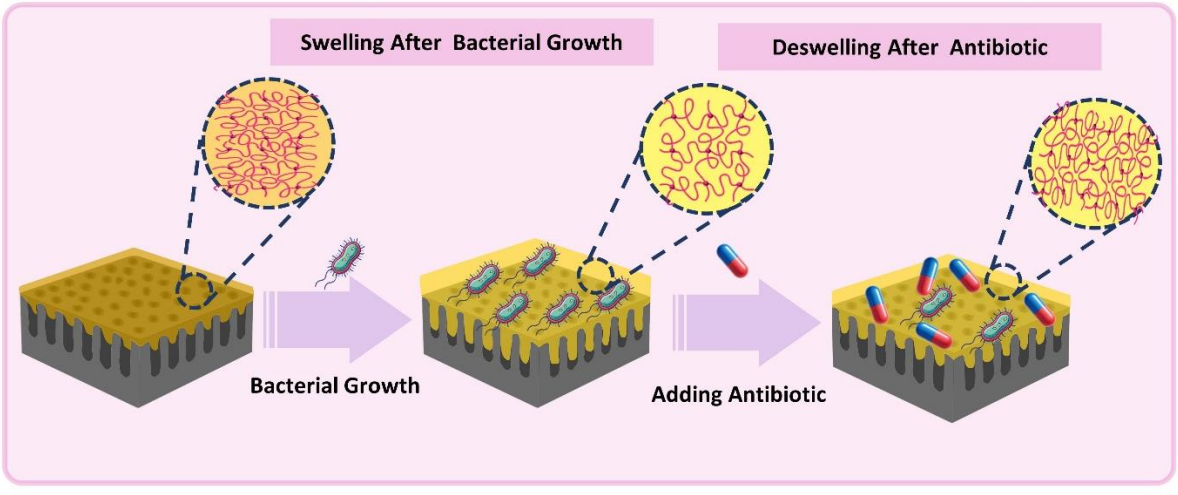


Figure 5. Proposed pH-sensing mechanism of the GIPSi nanosensor and its application to bacterial growth and antibiotic susceptibility detection.

3.3 RIFTS-based pH calibration

To investigate the pH responsiveness of the GIPSi, the evolution of the EOT signal was monitored under different buffer pH conditions. Initially, pH 7.4 buffer was introduced through both inlets of the Iμchip until a stable EOT baseline was established (~20 min). The buffer supplied to one inlet was then replaced with pH 6 buffer for another 20 min, while EOT was recorded every 30 s for all five GIPSi samples. **Fig. 6a** shows the changes in EOT relative to the baseline value measured in pH 7.4 for these sensors as a function of time. As expected, the sensor continuously exposed to the pH 7.4 buffer exhibited no significant change in EOT. In contrast, the EOT of the other sensors increased as the buffer pH was reduced from 7.4 to 6, consistent with the sensing mechanism proposed in Section 3.2.

As shown in **Fig. 6a** and **6b**, each experiment was performed in triplicate under identical conditions. The average EOT responses from the three independent experiments are presented in **Fig. 6c** as a function of buffer pH. A nonlinear relationship between the EOT change and buffer pH was observed over the investigated range. The experimental data were best fitted with a second-order polynomial model, yielding an R^2 value of 0.9951, indicating an excellent correlation between the sensor response and buffer pH. These results demonstrate the capability of the GIPSi platform for reliable optical monitoring of pH variations within the microfluidic chips.

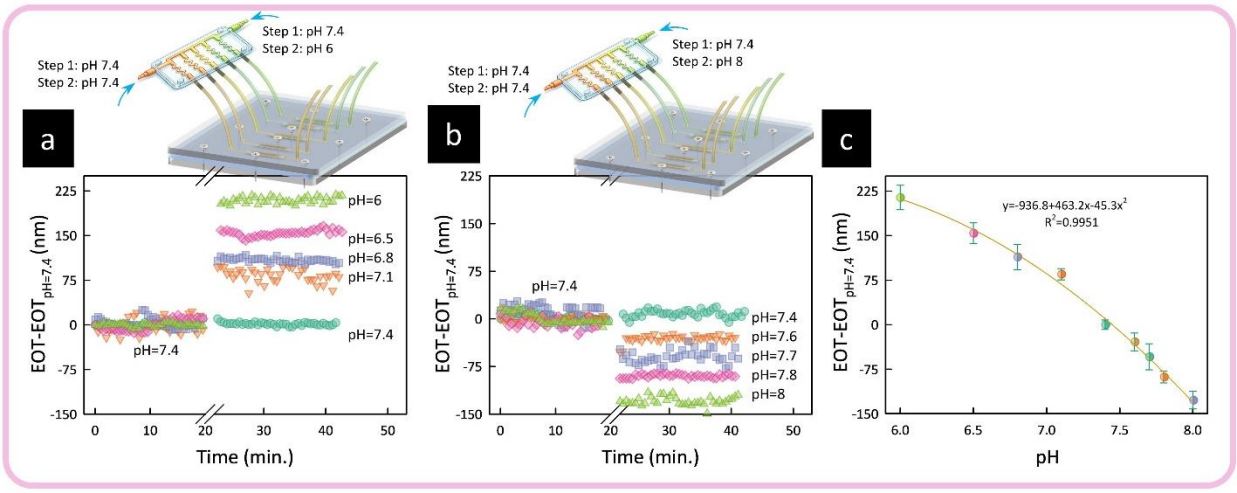


Figure 6. RIFTS response of the GIPSi-based sensor to various pH levels: (**a**) EOT changes over time during pH switches from 7.4 to 7.1, 6.8, 6.5, and 6. (**b**) EOT changes over time during pH switches from 7.4 to 7.6, 7.7, 7.8, and 8. (**c**) EOT calibration curve vs. pH (second-order polynomial fit, $R^2 = 0.9951$).

3.4 Measurement of bacteria-induced RIFTS changes

An *E. coli* suspension with a concentration of 1.5×10^8 CFU/mL was prepared and subsequently diluted with sterile culture medium to 25%, 50%, and 75% of the original concentration. Prior to incubation, the pH of the culture medium and all bacterial suspensions was adjusted to 7.4. The samples were then incubated at 37 °C, and the pH was measured every 30 min using a pH meter. The results are presented in **Fig. 7a**. For all bacterial suspensions, the pH decreased progressively during incubation, whereas the sterile culture medium control exhibited negligible pH variation, confirming that the observed acidification originated from bacterial metabolic activity rather than spontaneous changes in the culture medium. The pH–time profiles were well described by sigmoidal regression, with satisfactory coefficients of determination (R^2) obtained for all samples. This sigmoidal behavior is consistent with the characteristic growth kinetics of bacteria, where the pH decreases gradually during the lag

phase, more rapidly during the exponential growth phase as metabolic activity increases, and finally reaches a plateau in the stationary phase because of nutrient depletion and the accumulation of metabolic by-products [45,46].

Fresh culture medium adjusted to pH 7.4 was first introduced into the nanosensor μchip to establish a stable EOT baseline. Then, the five samples characterized in **Fig. 7a**—including four *E. coli* suspensions of different concentrations and one sterile culture-medium control, all collected after 8 h of incubation—were sequentially introduced into the nanosensor μchip, and the EOT was recorded at 30 s intervals. **Fig. 7b** shows the EOT response, expressed relative to the baseline value obtained with the pH 7.4 culture medium, for the GIPSi sensors located in the five microchannels as a function of time. The magnitude of the EOT shift (ΔEOT) increased with increasing initial bacterial concentration, indicating that higher bacterial loads produced greater metabolic acidification and, consequently, larger optical responses. The largest ΔEOT was observed for the undiluted bacterial suspension (100%, corresponding to 1.5×10^8 CFU/mL), whereas the sterile culture-medium control (0% bacteria) produced virtually no EOT shift ($\Delta EOT \approx 0$). These findings demonstrate that the GIPSi nanosensor is capable of transducing bacteria-induced metabolic acidification into a measurable optical signal.

To determine whether the observed optical responses were directly associated with pH changes induced by bacterial metabolism, the average ΔEOT values obtained from three independent experiments (performed as described for **Fig. 7b**) were plotted against the corresponding pH values measured after 8 h of incubation (**Fig. 7a**). These data were then compared with the calibration curve established using buffer solutions of known pH (**Fig. 6c**). The agreement between the experimental data and the values predicted by the quadratic calibration model was evaluated using the Pearson correlation coefficient [47]. A high correlation coefficient ($r = 0.987$) was obtained, indicating excellent agreement between the measured and predicted values. This

result confirms that the quadratic calibration accurately describes the sensor response over the investigated pH range. The close agreement between the bacterial data and the buffer calibration indicates that the optical response is governed predominantly by pH variations generated during bacterial metabolism, rather than by direct interactions of bacterial cells or their secreted products with the GIPSi sensor.

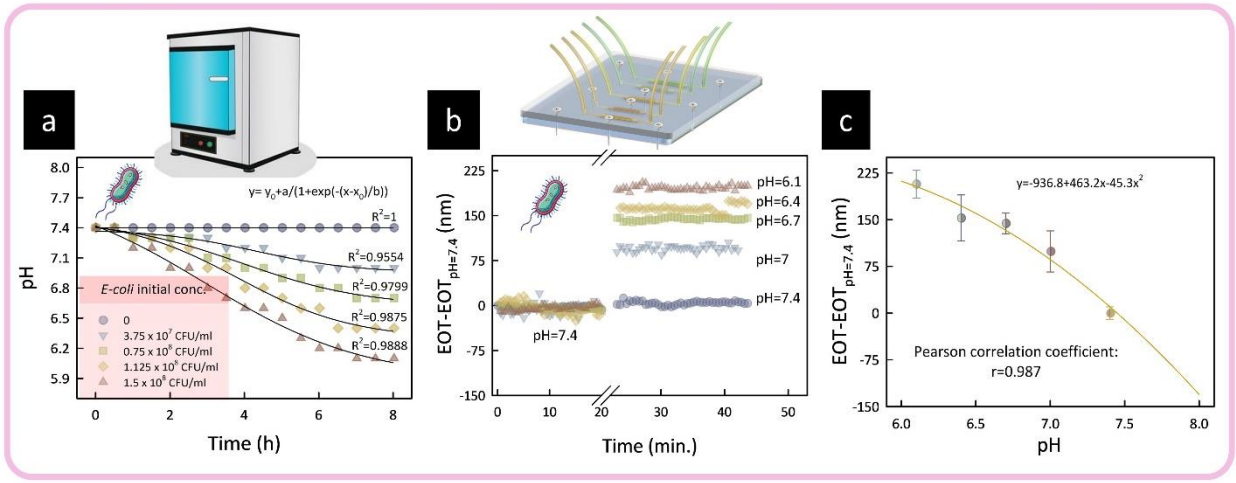


Figure 7. (**a**) pH changes of *E. coli* cultures at different concentrations over 8 h (sigmoidal fits). (**b**) RIFTS response of the GIPSi-based sensor to the samples of panel (**a**) after 8 h growth. (**c**) ΔEOT obtained from panel (**b**) after three replications vs. pH overlaid on the quadratic calibration curve (Figure 6c). The predicted and measured values show excellent agreement, with a Pearson correlation coefficient of r = 0.987.

3.5 Microfluidic AST

The results of the AST experiments performed using *E. coli* and the three antibiotics, CIP, GEN, and CEF, are presented in **Fig. 8**. Before performing the microfluidic AST experiments, the pH response of *E. coli* cultures to CIP, GEN, and CEF was first investigated under conventional bulk conditions. The concentration ranges for the three antibiotics were selected based on the experimentally determined minimum inhibitory concentration (MIC) of 0.74

468 µg/mL to encompass both sub-MIC and supra-MIC bacterial responses. The pH of the bulk
469 cultures was monitored every 30 min for 8 h at 37 °C. The resulting pH kinetic profiles are
470 presented in **Fig. 8a**, **8d**, and **8g**.

471 In all three cases, untreated control cultures (0 µg/mL) exhibited a rapid sigmoidal decline in
472 pH from 7.4 to approximately 6.0, reflecting active bacterial growth and the accumulation of
473 acidic metabolic by-products. Increasing the antibiotic concentration from 0.37 to 1.48 µg/mL
474 progressively reduced both the rate and the extent of pH decline in a dose-dependent manner.
475 Cultures exposed to 1.48 µg/mL of each antibiotic maintained pH values close to or above 7.4
476 throughout the incubation period, consistent with strong suppression of bacterial metabolic
477 activity. The sigmoidal regression model accurately described the pH kinetic profiles under
478 most conditions ($R^2 > 0.89$), confirming the robustness of the kinetic analysis. These findings
479 demonstrate that antibiotic-induced changes in bacterial metabolism provide an early
480 physiological indicator of antimicrobial susceptibility.

481 The small differences observed among the three antibiotics may be attributed to their distinct
482 mechanisms of antibacterial action. CIP, a fluoroquinolone, inhibits DNA gyrase and
483 topoisomerase IV, leading to the accumulation of DNA damage and bactericidal effects that
484 may produce heterogeneous metabolic responses before complete inhibition. GEN, an
485 aminoglycoside, irreversibly binds to the 30S ribosomal subunit, disrupting protein synthesis
486 and rapidly suppressing cellular metabolism. In contrast, CEF, a third-generation
487 cephalosporin, inhibits peptidoglycan cross-linking by binding to penicillin-binding proteins
488 (particularly PBP3 in Gram-negative bacteria), thereby impairing cell wall synthesis and
489 causing osmotic lysis during bacterial growth and division. The inhibition of metabolism
490 associated with β-lactam antibiotics likely contributes to the progressive suppression of
491 bacterial cell division, which is reflected by the gradual reduction in metabolic acidification
492 observed in the present study [48-50].

Following the bulk pH characterization, the microfluidic AST experiments were performed using the Iμchip. Initially, an *E. coli* suspension with a concentration of 1.5×10^8 CFU/mL adjusted to pH 7.4 was introduced through both inlets of the Iμchip until a stable baseline EOT was established for all GIPSi nanosensors (approximately 15 min). Subsequently, the solution supplied to one inlet was replaced with the same *E. coli* suspension containing the 1.48 μg/mL antibiotic concentration, also adjusted to pH 7.4, while the other inlet continued to receive the untreated bacterial suspension. This configuration generated a concentration gradient of the antibiotic within the CGG μchip. The syringe pumps were then stopped, allowing the bacterial suspensions to remain in contact with the antibiotic inside the CGG μchip for 1.5 h under static conditions. During this incubation period, the microfluidic platform was maintained at 37 °C. After incubation, the contents of the CGG μchip were driven into the nanosensor μchip and flowed across the GIPSi sensing elements for approximately 15 min, during which reflectance spectra were continuously acquired every 30 s and the corresponding EOT values were determined. **Fig. 8b**, **8e**, and **8h** present the ΔEOT responses, referenced to the baseline measured at pH 7.4, for the five sensing channels corresponding to CIP, GEN, and CEF, respectively. For all three antibiotics, lower concentrations produced relatively large positive ΔEOT values, consistent with the pronounced decrease in pH observed during active bacterial growth under weak antimicrobial inhibition. As the antibiotic concentration increased, the magnitude of ΔEOT progressively decreased, reflecting the reduced metabolic acidification associated with increasing inhibition of bacterial activity. Interestingly, at the highest antibiotic concentration (1.48 μg/mL), all three antibiotics produced negative ΔEOT values. According to the pH calibration established in Fig. 6c, negative ΔEOT values correspond to pH values higher than the baseline pH of 7.4. This observation is consistent with the bulk pH measurements (**Fig. 8a**, **8d**, and **8g**), in which the culture medium remained at or slightly above pH 7.4 under strong antibacterial inhibition.

To validate the reliability of the microfluidic assay against the conventional bulk method, the optical responses obtained from the microfluidic platform were quantitatively compared with the pH measurements obtained from bulk incubation experiments. First, the ΔEOT values obtained from the microfluidic experiments (**Fig. 8b**, **8e**, and **8h**) were converted into their corresponding pH values using the quadratic calibration curve established in **Fig. 6c**. The resulting pH values were then compared with the final pH values measured after 8 h of incubation under conventional bulk conditions (**Fig. 8a**, **8d**, and **8g**). The comparison is presented in **Fig. 8c**, **8f**, and **8i**. Both the conventional bulk assay and the microfluidic platform consistently identified low pH values (~6.1–6.2) in the absence of antibiotics and pH values approaching 7.4–7.7 at the highest antibiotic concentrations, demonstrating that the rapid microfluidic assay accurately captures the full range of bacterial susceptibility responses. A strong linear agreement was observed between the two approaches over the investigated concentration range, with Pearson correlation coefficients of $r = 0.921$ for CIP, $r = 0.921$ for GEN, and $r = 0.961$ for CEF, demonstrating excellent agreement between the microfluidic platform and the conventional bulk assay. Collectively, these findings validate the microfluidic platform as a rapid and reliable system for AST, capable of providing clinically relevant information on bacterial susceptibility within approximately one-fifth of the time required by conventional incubation methods.

The present approach differs fundamentally from conventional optical nanosensors that rely on direct bacterial capture or surface binding events. Instead, the GIPSi platform measures the metabolic consequences of bacterial growth through pH-dependent optical changes. Since metabolic inhibition represents one of the earliest physiological responses following exposure to effective antimicrobial agents, this strategy enables rapid assessment of antimicrobial susceptibility without requiring bacterial labeling, surface immobilization, or extended incubation periods.

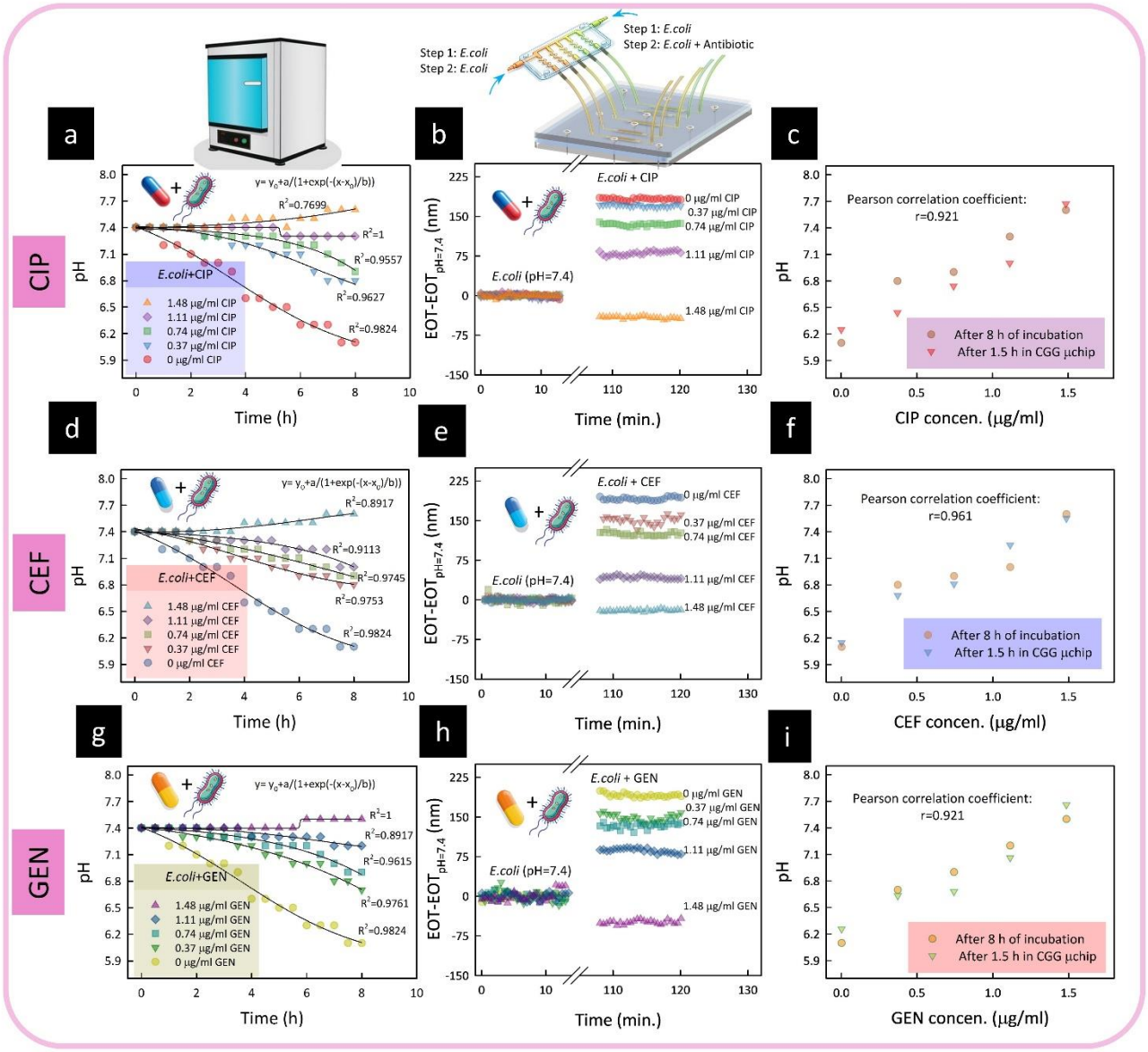


Figure 8. Rapid AST and metabolic monitoring of *E. coli* against CIP (a-c), CEF (d-f), and GEN (g-i). pH changes of *E. coli* cultures treated with different CIP (a), CEF (d) and GEN (g) concentrations over 8 h. Real-time RIFTS response of the Iµchip to the different concentration of CIP (b), CEF (e) and GEN (h). Comparison of pH values obtained after 8 h conventional incubation and after 1.5 h processing in the Iµchip for CIP (c), CEF (f) and GEN (i).

Conclusion

In this study, we developed and validated an integrated microfluidic–optical platform for rapid phenotypic antimicrobial susceptibility testing (AST) based on pH-responsive interferometric sensing. Scanning electron microscopy, energy-dispersive X-ray spectroscopy, and transfer matrix method simulations confirmed partial infiltration of gelatin into the PSi layer and demonstrated that the resulting optical response originated from pH-dependent swelling of the infiltrated gelatin within the porous matrix. The excellent agreement between the pH calibration established using buffer solutions and the bacteria-induced optical responses verified that bacterial metabolic acidification is the primary mechanism responsible for the observed EOT changes. By combining a concentration gradient generator microchip with a five-channel sensing microchip, the platform enabled on-chip generation of multiple antibiotic concentrations and their simultaneous incubation under identical conditions, reducing manual sample preparation, reagent consumption, and the overall assay workflow. The strong agreement between the 1.5 h microfluidic assay and the conventional 8 h incubation method for *E. coli* exposed to ciprofloxacin, gentamicin, and ceftazidime demonstrates that metabolic acidification provides a reliable early indicator of bacterial susceptibility. Overall, the proposed label-free platform integrates rapid microfluidic analysis with parallel optical sensing, offering a simple, low-volume, and potentially clinically translatable approach for accelerated phenotypic antimicrobial susceptibility testing.

Data availability

All data supporting the findings of this study are included in the article and its supplementary information and Supplementary Video. No additional source data are required.

Acknowledgements

This work was supported by the Center for International Scientific Studies and Collaboration (CISSC), Ministry of Science, Research and Technology of Iran, and the Iran National Science Foundation (INSF) under Project No. 4025831, as well as by the Scientific and Technological Research Council of Türkiye (TÜBİTAK) under Project No. 122N806, entitled “Rapid Antibiotic Susceptibility Testing by Reflectance Measurement Using Hydrogel-Coated Porous Silicon in a Microfluidic System.

Conflict of interests

The authors declare no competing interests.

Author details

[1] Department of Nanobiotechnology and Biomimetics, School of Life Science Engineering, College of Interdisciplinary Science and Technology, University of Tehran, Tehran, Iran. [2] Department of Microbiology, Faculty of Medicine, Mustafa Kemal Hatay University, Antakya-Hatay, Turkey. [3] Department of Medical Technology and Tissue Engineering, School of Life Science Engineering, College of Interdisciplinary Science and Technology, University of Tehran, Tehran, Iran. [4] Converging Technologies Research Center, Shahid Beheshti University, Tehran, Iran. [5] Department of Histology and Embryology, Faculty of Medicine, Mustafa Kemal Hatay University, Antakya-Hatay, Turkey.

Author contributions

Conceptualization: Rahimi, Duran, Abouei, and Sedighi; Methodology: Rahimi, Duran, Abouei, and Sedighi; Software: Rahimi, Abouei, and Mosayebzadeh; Validation: Rahimi, Duran, Abouei, and Sedighi; Formal analysis: Rahimi, Duran, Abouei, Abarghoe, and Mosayebzadeh; Investigation: Abarghoe, Mosayebzadeh, Elif Yaprak Colak, and Selin Sabanci; Resources: Rahimi; Data curation: Rahimi and Abarghoe; Writing – original draft: Abarghoe and Mosayebzadeh; Writing – review and editing: Rahimi, Duran, Abouei, and

Sedighi; Visualization: Rahimi, Abouei, Abarghoe, and Mosayebzadeh; Supervision: Rahimi; Project administration: Rahimi; Funding acquisition: Rahimi and Duran. All authors reviewed and approved the final manuscript.

Supplementary information accompanies the manuscript on the Microsystems & Nanoengineering website (http://www.nature.com/micronano).

References

1. Duran, N., Ozer, B., Duran, G. G., Onlen, Y. & Demir, C. Antibiotic resistance genes & susceptibility patterns in staphylococci. *Indian J. Med. Res.* **135**, 389-396 (2012).
2. Bayraktar, H. S. *et al.* Disinfectant/antiseptic resistance genes of Staphylococci and serotyping of clinical Staphylococcus aureus isolates. *J Infect Dev Ctries* **20**, 219-228 (2026).
3. Zhang, K., Qin, S., Wu, S., Liang, Y. & Li, J. Microfluidic systems for rapid antibiotic susceptibility tests (ASTs) at the single-cell level. *Chemical Science* **11**, 6352-6361 (2020).
4. Global burden of bacterial antimicrobial resistance 1990-2021: a systematic analysis with forecasts to 2050. *Lancet* **404**, 1199-1226 (2024).
5. Yaprak Çolak, E. & Duran, N. Synergistic antibacterial effects of postbiotics combined with linezolid and amikacin against nosocomial pathogens. *Front Cell Infect Microbiol* **15** (2025).
6. Khan, Z. A., Siddiqui, M. F. & Park, S. Current and Emerging Methods of Antibiotic Susceptibility Testing. *Diagnostics (Basel)* **9** (2019).
7. Kaprou, G. D., Bergšpica, I., Alexa, E. A., Alvarez-Ordóñez, A. & Prieto, M. Rapid Methods for Antimicrobial Resistance Diagnostics. *Antibiotics (Basel)* **10** (2021).
8. Reszetnik, G. *et al.* Publisher Correction: Next-generation rapid phenotypic antimicrobial susceptibility testing. *Nat Commun* **16**, 2805 (2025).
9. Galvan, D. D. & Yu, Q. Surface-enhanced raman scattering for rapid detection and characterization of antibiotic-resistant bacteria. *Adv. Healthc. Mater.* **7**, 1701335 (2018).

10. Kasas, S. *et al.* Nanomotion detection-based rapid antibiotic susceptibility testing. *Antibiotics* **10**, 287 (2021).
11. Novelli-Rousseau, A. *et al.* Culture-free antibiotic-susceptibility determination from single-bacterium Raman spectra. *Sci. Rep.* **8**, 3957 (2018).
12. Tannert, A., Grohs, R., Popp, J. & Neugebauer, U. Phenotypic antibiotic susceptibility testing of pathogenic bacteria using photonic readout methods: recent achievements and impact. *Appl. Microbiol. Biotechnol.* **103**, 549-566 (2019).
13. Ibarlucea, B. *et al.* Nanowire sensors monitor bacterial growth kinetics and response to antibiotics. *Lab Chip* **17**, 4283-4293 (2017).
14. Kuss, S. *et al.* Versatile electrochemical sensing platform for bacteria. *Anal. Chem.* **91**, 4317-4322 (2019).
15. Ryser, T. *et al.* A microfluidic platform for whole-membrane integrity profiling in live neuronal cells. *Microsyst. Nanoeng.* **12** (2026).
16. Zhou, P. *et al.* A smartphone-powered decentralized microfluidic platform for sensitive CRISPR-based nucleic acid detection. *Microsyst. Nanoeng.* **12**, 212 (2026).
17. Kwon, D.-I. *et al.* Microfluidic–optical integrated portable platform with handheld pump for wash-free plasmonic detection of thrombin and SARS-CoV-2 spike protein. *Microsyst. Nanoeng.* **12** (2026).
18. Shi, H. *et al.* Rapid and steady concentration gradient generation platform for an antimicrobial susceptibility test. *Chem. Eng. J.* **359**, 1327-1338 (2019).
19. Heuer, C. *et al.* A 3D-printed microfluidic gradient generator with integrated photonic silicon sensors for rapid antimicrobial susceptibility testing. *Lab Chip* **22**, 4950-4961 (2022).
20. Ma, J. *et al.* Hydrogel sensors for biomedical electronics. *Chem. Eng. J.* **481**, 148317 (2024).
21. Sun, X., Agate, S., Salem, K. S., Lucia, L. & Pal, L. Hydrogel-based sensor networks: Compositions, properties, and applications—A review. *ACS Appl. Bio Mater.* **4**, 140-162 (2020).
22. Sun, X., Ding, C., Qin, M. & Li, J. Hydrogel-based biosensors for bacterial infections. *Small* **20**, 2306960 (2024).

651 23. Deen, G. R. & Loh, X. J. Stimuli-responsive cationic hydrogels in drug delivery applications.
652 *Gels* **4**, 13 (2018).
653 24. Samal, S. K. *et al.* Cationic polymers and their therapeutic potential. *Chem. Soc. Rev.* **41**, 7147-
654 7194 (2012).
655 25. Taokaew, S., Kaewkong, W. & Kriangkrai, W. Recent development of functional chitosan-
656 based hydrogels for pharmaceutical and biomedical applications. *Gels* **9**, 277 (2023).
657 26. Ofridam, F. *et al.* pH-sensitive polymers: Classification and some fine potential applications.
658 *Polym. Adv. Technol* **32**, 1455-1484 (2021).
659 27. Tang, Y., Zhen, L., Liu, J. & Wu, J. Rapid antibiotic susceptibility testing in a microfluidic pH
660 sensor. *Anal. Chem.* **85**, 2787-2794 (2013).
661 28. Yaghoubi, M., Rahimi, F., Negahdari, B., Rezayan, A. H. & Shafiekhani, A. A lectin-coupled
662 porous silicon-based biosensor: label-free optical detection of bacteria in a real-time mode. *Sci*
663 *Rep* **10**, 16017(2020).
664 29. Mohammadi, S. *et al.* Design, fabrication, and characterization of microfluidic-based
665 interferometric porous silicon aptasensors for multiplexed sepsis biomarkers detection. S*ens.*
666 *Actuators Rep.* **10**, 100382 (2025).
667 30. Aliabadi, F. *et al.* rHuEPO-α Biosensing by Porous Silicon Integrated into Microchannels via
668 Reflectometric Interference Fourier Transform Spectroscopy. *Anal.l Chem* **97** (2025).
669 31. Awawdeh, K., Buttkewitz, M. A., Bahnemann, J. & Segal, E. Enhancing the performance of
670 porous silicon biosensors: the interplay of nanostructure design and microfluidic integration.
671 *Microsyst. Nanoeng.* **10**, 100 (2024).
672 32. Abarghoe, S., Rahimi, F., Duran, N., Abouei Mehrizi, A. & Sedighi, M. Design and Fabrication
673 of Porous Silicon-Gelatin Hybrid to Detect Bacterial Growth by Reflectometric Interference
674 Fourier Transform Spectrometry. *Iran. J. Polym. Sci. Technol* **37** (2024).
675 33. Wu, J. & Sailor, M. J. Chitosan Hydrogel-Capped Porous SiO2 as a pH Responsive Nano-
676 Valve for Triggered Release of Insulin. *Adv. Funct. Mater.* **19**, 733-741 (2009).

34. Mugnaini, G., Gelli, R., Mori, L. & Bonini, M. How to cross-link gelatin: The effect of glutaraldehyde and glyceraldehyde on the hydrogel properties. *ACS Appl. Polym. Mater.* **5**, 9192-9202 (2023).

35. Mosayebzadeh, M., Abouei Mehrizi, A. Design, Fabrication, and Evaluation of a Microfluidic Concentration Gradient-Generating Chip for Biological and Biomedical Applications. (2024).

36. Haley, E. *et al.* Pooled antibiotic susceptibility testing performs within CLSI standards for validation when measured against broth microdilution and disk diffusion antibiotic susceptibility testing of cultured isolates. *Antibiotics* **13**, 1214 (2024).

37. Schuetz, A. N., Ferrell, A., Hindler, J. A., Humphries, R. & Bobenchik, A. M. Overview of changes in the Clinical and Laboratory Standards Institute performance standards for antimicrobial susceptibility testing: M100 32nd and 33rd editions. *J. Clin. Microbiol.* **63**, e01623-01623 (2025).

38. Buhl, M. *et al.* External quality assessment in antimicrobial susceptibility testing (EUCAST disc diffusion methodology) of five anaerobic strains–performance of 35 laboratories in Germany and Austria, 2024. *Anaerobe*, 103025 (2026).

39. Yeh, P. *Optical Waves in Layered Media* (Wiley, 2006).

40. Theiß, W. Optical properties of porous silicon. *Surf. Sci. Rep.* **29**, 91-192 (1997).

41. Khardani, M., Bouaïcha, M. & Bessaïs, B. Bruggeman effective medium approach for modelling optical properties of porous silicon: comparison with experiment. *Phys. Status Solidi C* **4**, 1986-1990 (2007).

42. Calixto, S., Ganzherli, N., Gulyaev, S. & Figueroa-Gerstenmaier, S. Gelatin as a Photosensitive Material. *Molecules* **23**, doi:10.3390/molecules23082064 (2018).

43. Milano, F. *et al.* Current Trends in Gelatin-Based Drug Delivery Systems. *Pharmaceutics* **15**, doi:10.3390/pharmaceutics15051499 (2023).

44. Riedel, S., Heyart, B., Apel, K. S. & Mayr, S. G. Programing stimuli-responsiveness of gelatin with electron beams: basic effects and development of a hydration-controlled biocompatible demonstrator. *Sci. Rep* **7**, 17436, doi:10.1038/s41598-017-17734-y (2017).

45. Zwietering, M. H., Jongenburger, I., Rombouts, F. M. & Van't Riet, K. Modeling of the bacterial growth curve. *Appl. Environ. Microbiol.* **56**, 1875-1881 (1990).

46. Pla, M.-L., Oltra, S., Esteban, M.-D., Andreu, S. & Palop, A. Comparison of primary models to predict microbial growth by the plate count and absorbance methods. Appl. Environ. Microbiol**. 2015**, 365025 (2015).

47. Durrheim, K. & Tredoux, C. *Numbers, hypotheses & conclusions: A course in statistics for the social sciences*. (Juta and Company Ltd, 2004).

48. Kakoullis, L., Papachristodoulou, E., Chra, P. & Panos, G. Mechanisms of antibiotic resistance in important gram-positive and gram-negative pathogens and novel antibiotic solutions. *Antibiotics* **10**, 415 (2021).

49. Munita, J. M. & Arias, C. A. Mechanisms of antibiotic resistance. (*Virulence mechanisms of bacterial pathogens,* 2016).

50. Darby, E. M. *et al.* Molecular mechanisms of antibiotic resistance revisited. *Nat. Rev. Microbiol.* **21**, 280-295 (2023).

Supplementary Files

This is a list of supplementary files associated with this preprint. Click to download.

- Scheme.3.jpg
- SupplementaryinformationRapidASTbyRIFTSonGIPSiIntegratedintoMicrochips.docx
- Supplementaryvideo.mov